J. Fluid Mech. (2010), *vol.* 645, *pp.* 345–373. © Cambridge University Press 2010
doi:10.1017/S0022112009992941

Computational modelling and analysis of the hydrodynamics of a highly deformable fish pectoral fin

H. DONG[1]†, M. BOZKURTTAS[1], R. MITTAL[1]‡,
P. MADDEN[2] AND G. V. LAUDER[2]

[1]Department of Mechanical and Aerospace Engineering, The George Washington University 801 22nd St. NW, Washington DC 20052, USA

[2]The Museum of Comparative Zoology, 26 Oxford Street, Harvard University, Cambridge, MA 02138, USA

(Received 11 February 2009; revised 20 October 2009; accepted 20 October 2009;
first published online 8 February 2010)

Numerical simulations are used to investigate the flow associated with a bluegill sunfish (*Lepomis macrochirus*) pectoral fin during steady forward motion. The simulations are intended to match the experiments of Lauder *et al.* (*Bioinsp. Biomim.*, vol. 1, 2006, p. S25), and the results obtained from the simulations complement the experimental analysis. The focus of the current paper is on the quantitative characterization of the propulsive performance of the pectoral fin, which undergoes significant deformation during its stroke. This includes a detailed analysis of the thrust production mechanisms as well as their connection to the vortex dynamics and other flow features. The simulations indicate that the fish fin produces high propulsive performance by employing a complex fin gait driven by active and passive fin deformation. By connecting the vortex dynamics and fin kinematics with the surface distribution of the force on the fin, it is found that during abduction, the fin moves such that the tip of the fin undergoes a complex, three-dimensional flapping motion that produces a strong and long-lasting, attached tip vortex. This tip vortex is associated with most of the thrust production during the abduction phase of the stroke. During the adduction phase, the fin motion is similar to a ‘paddling’ stroke. Comparisons are made with rigid flapping foils to provide insights into the remarkable performance of the fish fin and to interpret the force production from the viewpoint of functional morphology.

1. Introduction

The current paper describes the computational modelling and analysis of the hydrodynamics of a highly deformable fish pectoral fin. In this study, we focus on the steady swimming of the bluegill sunfish (*Lepomis macrochirus*) at a speed of about 1.1 body lengths per second (BL s^{-1}). It is known (Drucker & Lauder 2000; Lauder *et al.* 2006) that up to these speeds, these fish usually use their pectoral fins exclusively

---

† Present address: 126 Russ Center, Wright State University, 3640 Colonel Glenn Highway, Dayton, OH 45435, USA.

‡ Present address: 126 Latrobe Hall, Johns Hopkins University, 3400 North Charles Street, Baltimore, MD 21218-2686, USA. Email address for correspondence: mittal@jhu.edu

for generating the required propulsive forces. Thus, limiting our study to these speeds allows us to focus on labriform propulsion, and eliminates the confounding effects associated with the motion of other fins and the body. The kinematics of the pectoral fin of the bluegill sunfish and the experimental hydrodynamic studies have been described in detail by Lauder *et al.* (2006). In particular, the experiments have documented in detail the pectoral fin kinematics during steady forward swimming and have provided qualitative as well as some quantitative information regarding the hydrodynamics. Figure 1 shows experimental visualizations of the fin kinematics which clearly highlight the complex motion and significant deformation of the fin.

A detailed experimental examination of the kinematics shows that the fin undergoes large-scale active as well as flow-induced deformation during its flapping cycle, and the kinematics cannot easily be categorized into the conventional view of rowing versus flapping kinematics. Consequently, the thrust production of this fin also cannot be easily ascribed to drag- or lift-based mechanisms (Walker & Westneat 2000; Mittal 2004). The experimental visualizations indicate that the typical pectoral fin gait adopted, when this fish swims between about 0.5 and 1.1 $\mathrm{BL\,s^{-1}}$ is such that during the abduction (outward) stroke, vortices are produced at both the dorsal and ventral leading edges of the fin. Leading-edge vortices are also created during the adduction (inward) stroke. Particle image velocimetry (PIV) measurements at selected planes are used to construct a view of the complex vortex field that appears in the wake at the end of one flapping cycle.

Estimates of the thrust and the lateral forces generated by the fin during the cycle are also obtained by two different means. In the first method, the acceleration of the fish body during the stroke is determined from the image-correlation analysis, which is used to extract an estimate of the forces produced during the fin stroke. The second method relies on a control-volume analysis of the flow around the fin and produces an estimate based on the momentum flux through this control volume. The experimental estimates indicate that peaks in thrust are created during the abduction as well as the adduction strokes. However, both the vertical and spanwise forces show positive peaks during abduction and negative peaks during the adduction stroke. Furthermore, the magnitude of the peak lateral forces produced by the fin is very comparable (and usually lower) than the thrust peak. This is found to be in direct contrast to rigid three-dimensional flapping foils (Triantafyllou, Triantafyllou & Grosenbaugh 1992; Techet *et al.* 2005; Dong, Mittal & Najjar 2006) in which the peak vertical forces are usually found to be higher by a factor of three or more than the peak thrust forces. This has two important implications. First, given that fish in general and bluegill sunfish in particular are inherently unstable, reduced oscillatory lateral forces help the fish to maintain stability. The reduced amplitude of lateral forces also lead to a lower level of body oscillations and provide the fish with a relatively stationary visual platform.

The second implication of this observation is that the fish fin likely has a relatively high propulsive efficiency. In the current context, propulsive efficiency is defined as

$$\eta = \frac{\bar{P}_{out}}{\bar{P}_{in}}, \tag{1.1}$$

where $\bar{P}_{out}$ is the mean useful power produced by the fin over one stroke and $\bar{P}_{in}$ is the mean total power input to the fin over the stroke. The mean useful power is equal to $\bar{T}U_\infty$ where $\bar{T}$ is the mean thrust produced by the fin and U_∞ is the mean forward velocity of the fish. If $\boldsymbol{\sigma}$ is the traction over the fin surface, then the mean thrust is

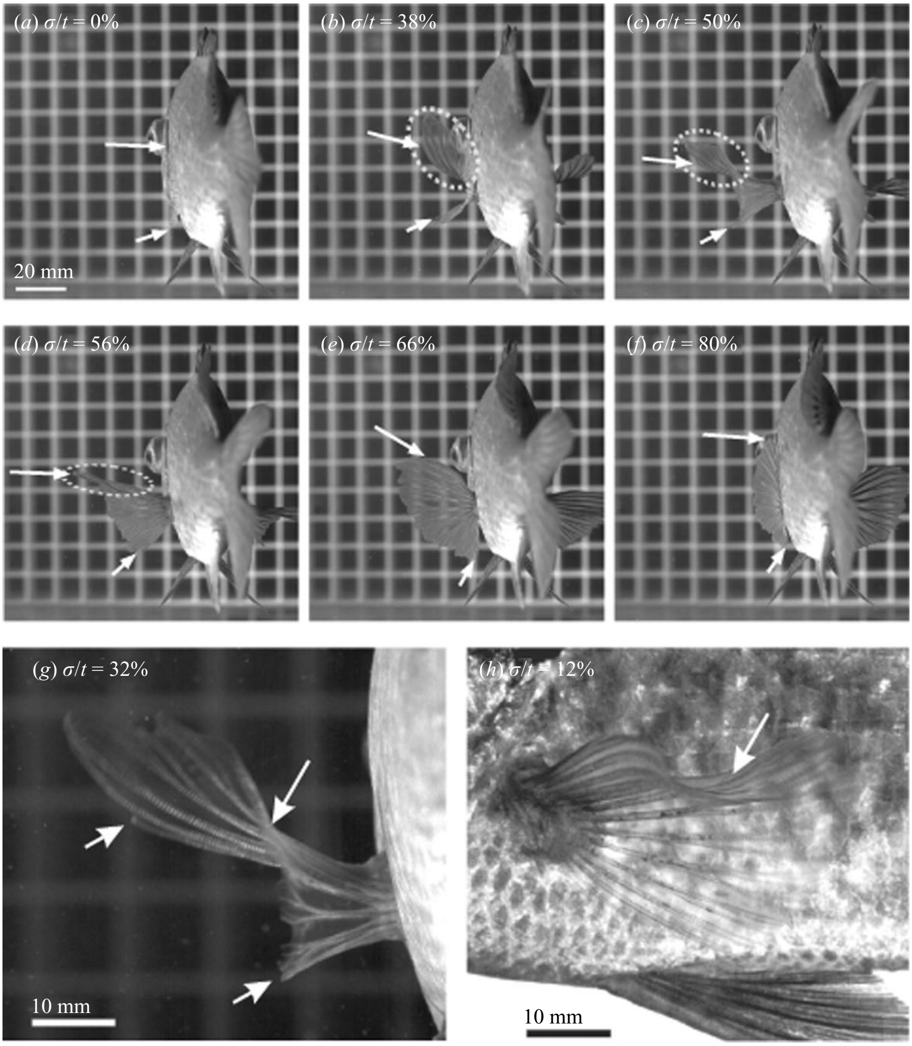

FIGURE 1. Views of pectoral fin motion during steady swimming by bluegill sunfish (images represent individual frames from a 250 Hz high-speed video sequence). Arrows indicate positions of the dorsal (long arrows) and ventral (short arrows) fin rays. (*a*) $t = 0.0\tau$ ($\tau =$ beat period). At the start of the beat, all the fin rays are against the fish body. (*b*) $t = 0.38\tau$. During the outstroke, the dorsal rays move away from the body and downward. As the dorsal rays drop during the outstroke, the distal ends of these fin rays bend upward increasing the area normal to the flow, highlighted by the dashed oval in this and the next three images. The ventral fin rays also move away from the body and the fin takes on a cupped shape. There is very little area normal to the flow in the ventral half of the fin. (*c*) $t = 0.50\tau$. The dorsal and ventral edges are at maximum outstroke. The dorsal half of the fin has rotated from a vertical orientation at the beginning of the stroke towards a horizontal orientation. (*d*) $t = 0.56\tau$. The dorsal and ventral edges begin to separate as the fin transitions from the outstroke to the instroke. (*e*) $t = 0.66\tau$. The dorsal and ventral edges have moved apart and the fin surface is nearly flat. (*f*) $t = 0.80\tau$. The fin has nearly returned to the body. (*g*) Close view of the fin and fin rays at 0.32τ to illustrate the cupped fin conformation with the upper and lower fin margins (small arrows) and the trailing central fin region (large arrow). (*h*) Side view of the fin at 0.12τ to show the wave of bending that propagates out along the upper fin margin (arrow).

given by

$$\bar{T} = \frac{1}{m\tau}\int_{m\tau}\int_{A_{fin}} \sigma_1 \mathrm{d}A\,\mathrm{d}t, \tag{1.2}$$

where τ is the time period of one stroke, m is the number of strokes over which the mean is computed and σ_1 is the component of the surface traction in the direction of thrust. The total mean mechanical input power to the fin can then be computed as

$$\bar{P}_{in} = \frac{1}{m\tau}\int_{m\tau}\int_{A_{fin}} (\boldsymbol{\sigma}\cdot\boldsymbol{V})\,\mathrm{d}A\,\mathrm{d}t, \tag{1.3}$$

where $\boldsymbol{V}$ is the local velocity of the fin surface. The above expression can be expanded as follows:

$$\bar{P}_{in} = \bar{T}U_\infty + \bar{P}_p, \tag{1.4}$$

where $\bar{P}_p$ is the 'parasitic' or wasted work done by the lateral forces and is computed as follows

$$\bar{P}_p = \frac{1}{m\tau}\int_{m\tau}\int_{A_{fin}} (\sigma_1' v_1' + \sigma_2 V_2 + \sigma_3 V_3)\,\mathrm{d}A\,\mathrm{d}t, \tag{1.5}$$

where σ_2 and σ_3 are the components of the surface traction perpendicular to the thrust, V_2 and V_3 are the corresponding surface velocities, and σ_1' and v_1' are the fluctuations from the mean values of the surface traction and the local fin velocity, respectively, in the direction of motion:

$$\eta = \frac{1}{1+\bar{P}_p/\bar{T}U_\infty} \tag{1.6}$$

Thus, a reduction in the magnitude of lateral forces and/or the time variation in the thrust force would produce lower values of $\bar{P}_p$ and, consequently, lead to a higher propulsive efficiency. However, since it is difficult to measure the power input $\bar{P}_{in}$ to the fin experimentally, it is not possible to obtain a reasonably accurate measure of efficiency from experiments. On the other hand, computational simulations of the hydrodynamics of this pectoral fin allow us to compute this key quantity. Simulations also provide the distribution of quantities on the fin surface as well as full-field information regarding velocity, pressure and vorticity, which would allow us to determine the mechanisms of thrust production as well as to determine the connection between fin characteristics (such as kinematics and planform) and fin performance. This is the primary motivation for the computational effort that is the subject of the current paper.

High-fidelity computational modelling of a configuration such as the bluegill pectoral fin is a highly challenging proposition. First, it involves a highly deformable, three-dimensional moving boundary, and a computational methodology that is capable of addressing this aspect of the fin is needed. Second, the flow Reynolds number for the fin is $O(10^3)$ which is high enough so as to require high-density grids and large computational times. Finally, the dynamics of the flow are dominated by distinct and rapidly interacting vortex structures, and our ability to extract insight regarding the underlying hydrodynamics mechanisms requires a numerical method and an accuracy level that can adequately resolve this vortex dynamics in space and time.

Although there are a number of computational studies that have examined both two-dimensional (Tuncer, Walz & Platzer 1998; Ramamurti & Sandberg 2001; Lewin & Haj-Hariri 2003) and three-dimensional rigid flapping foils (Blondeaux *et al.* 2005; Techet *et al.* 2005; Dong *et al.* 2006), the level of complexity inherent in the current study exceeds these past studies. Of particular note here is the study by Ramamurti *et al.* (2002) in which an unstructured grid-based method was used to simulate the flow associated with the pectoral fin of a bird-wrasse. The simulations employed an adaptive re-meshing technique coupled with an arbitrary Lagrangian Eulerian (ALE) formulation to solve the Navier–Stokes equations for a bird-wrasse fin during steady forward swimming. However, as noted by Walker & Westneat (1997) and Ramamurti *et al.* (2002), the essential kinematics of the bird-wrasse pectoral fin are similar to the flapping of insect wings during flight and involve a pitching and rolling motion initiated by the leading-edge fin ray. The fin is held out into the flow during the stroke and the anterior/posterior motion of the fin is relatively small. The fin does exhibit deformation, but this is also relatively small and is mostly limited to a deformation in the chordwise direction. The kinematics of the wrasse-fin were obtained by tracking the coordinates of five markers on the leading and trailing edges of the fin with simultaneous lateral and dorsal images of the fin obtained by a video camera. The simulations were carried out for a case for which the stroke frequency (f) was 3.3 Hz and the forward speed of the fish (U_{fish}) was $45\,\mathrm{cm\,s^{-1}}$. Estimating the spanwise length of the fin (L_{fin}) to be about 3.5 cm from Walker & Westneat (1997) and Ramamurti *et al.* (2002), the Reynolds number for the fin, defined as $L_{fin}U_{fish}/\nu_{water}$, was about 16 000. Furthermore, the Strouhal number, defined as fL_{fin}/U_{fish}, was about 0.26. Given that the fin underwent about a 122° total angular motion at the root, we estimate the ratio of tip amplitude to fin span to be about 1.74. The thrust and lift forces were computed from the surface force distribution and analysed with respect to the flow patterns. Since no flow measurements were conducted in the experiments, no direct comparison of the computational and experimental forces was possible. However, the experiments did measure body accelerations, which were used to provide some level of confirmation for trends observed in the computed forces. Estimates of propulsive efficiency were not provided in this work.

The key difference between this previous work and the current effort is that the extent of deformation of the bluegill fin is significantly higher than that seen for the bird-wrasse, and this has significant implications for the computational modelling of this fin. First, a significantly larger number of surface points needs to be tracked on the fin in order to be able to recreate the kinematics in the computational model. Second, the temporal resolution of the kinematical data should be high enough so as not to miss any key features of the fin gait. The large level of deformation also adds further challenges for the computations since it requires the use of a numerical methodology that is capable of dealing with large surface deformations.

The methodology used to develop a high-fidelity computational model of the pectoral fin hydrodynamics has been described in detail by Bozukurttas *et al.* (2009) and only a brief description of this is provided. It should be noted that this previous paper also described certain aspects of the hydrodynamics of this pectoral fin. The focus there was to extract insights that would be particularly relevant to the design of a bioinspired engineered fin. Proper orthogonal decomposition (POD) was used to decompose the complex fin kinematics, and simple fin gaits synthesized from these modes were subjected to computational fluid dynamics (CFD) modelling in order to determine those components of the kinematics that are most essential for the fin performance. The study also examined the effect of size and frequency on the fin performance via a Reynolds and Strouhal number variation.

While the study described here uses precisely the same CFD technique to examine the hydrodynamics of the bluegill pectoral fin, the focus of this paper is on establishing the flow mechanisms that determine the propulsive performance of the fish fin. The hydrodynamic forces computed in the simulations are compared with estimates from companion experimental measurements in order to assess the fidelity level of the simulations. The propulsive efficiency is determined from the computed forces, and this represents the first time, to our knowledge, that such a determination has been made for a fish pectoral fin. The computed velocity, pressure and vorticity fields are examined in detail in order to determine the hydrodynamic features and mechanisms that are key for producing thrust. The role of fin deformation and fin planform on the force production by the fin is also deduced from an examination of the surface forces and flow, and the vorticity field in the vicinity of the fin. A detailed comparison of the fish fin performance is also made with available data on rigid flapping foils in order to assess the extent to which the fish fin out(under)performs engineered designs. Finally, based on our computations and experiments, we comment on the overall hydrodynamic performance of the fin and its implications for functional morphology as well as for bio-inspired engineering designs of flapping foil propulsors.

2. Bluegill sunfish pectoral fin kinematics

The method used to digitize the bluegill sunfish's pectoral fin kinematics during steady forward motion is described by Lauder *et al.* (2006) and Bozukurttas *et al.* (2009), but the key features of this methodology are included here for the sake of completeness.

The fin position through time was digitized using high-speed, high-resolution videos, fully calibrated (Stacoff *et al.* 1996; Hsieh 2003; Standen & Lauder 2005) from two orthogonal (ventral and lateral) views using Photron FastCam 1024 PCI cameras. The images were taken at 500 frames per second, with a resolution of 1024×1024 pixels. Three-dimensional fin geometry was measured by digitizing the ventral and lateral camera views. About 20 frames and 200 points per frame were digitized for one individual fish. This original surface mesh is used as a basis for reconstructing a significantly higher resolution surface mesh required for CFD. Details of this surface mesh can be found in Bozukurttas *et al.* (2009).

Three phases (abduction, adduction and intermediate) of pectoral fin movement were observed in the bluegill's steady forward motion. Although the abduction and adduction phases were digitized, the intermediate phase could not be digitized because of the lack of a full view of all the rays when the fin was right up against the body. The length of the intermediate phase was also variable and ranged from virtually none to a second or more. Fortunately, this phase is not dynamically significant since given the fin position, it likely does not produce any forces during this phase. Thus, our inability to model this phase of the stroke is not expected to have any significant effect on the predicted hydrodynamics. The abduction and adduction phases are demonstrated in figure 2 via snapshots using two views of the fin beat cycle.

High-resolution digital videos of fish pectoral fin motion during locomotion reveal that the pectoral fins of bluegill sunfish are highly flexible. Fish have active muscular control over the leading and trailing edges of their fins through adductor and abductor muscles. These muscle groups have individual bundles that insert on the base of each individual bony fin ray that supports the fin (Lauder & Madden 2006). As a result, during locomotion fish pectoral fins exhibit: (i) changes in area, (ii) bending in both chordwise and spanwise directions, (iii) distinct correlated movement of the upper (dorsal) and the lower (ventral) edges (while the middle of the fin often lags behind),

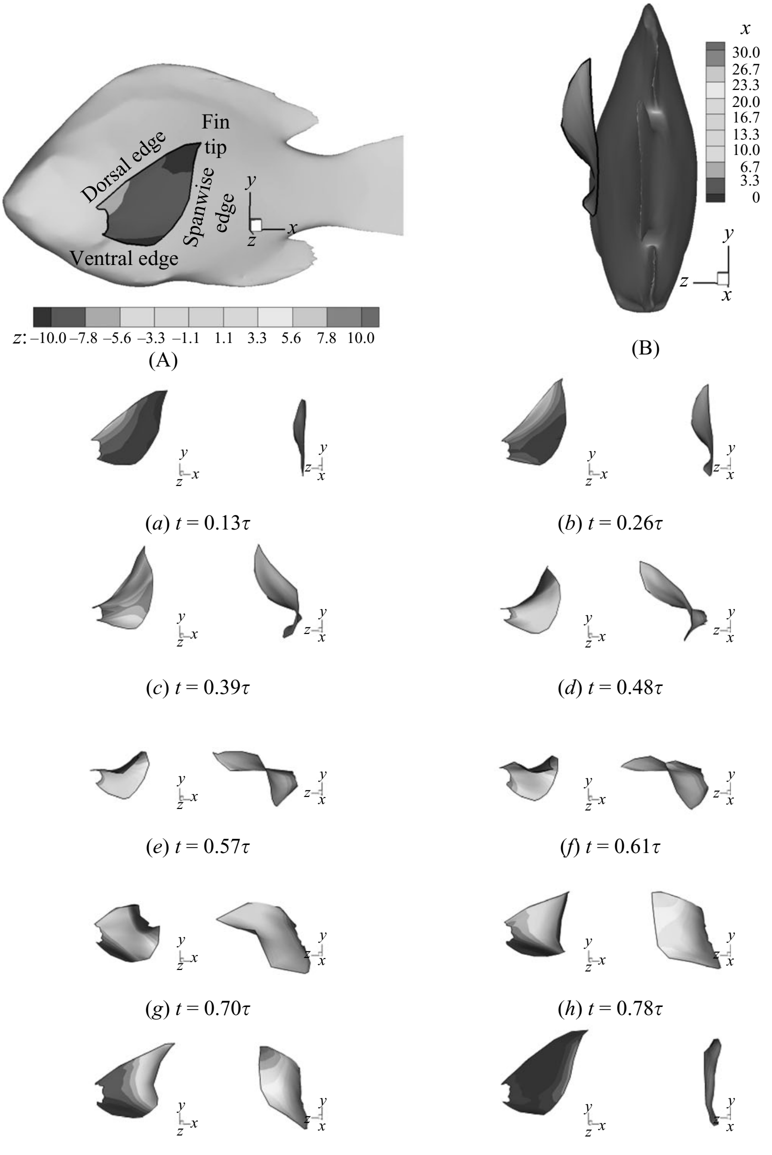

(*a*) $t = 0.13\tau$ (*b*) $t = 0.26\tau$

(*c*) $t = 0.39\tau$ (*d*) $t = 0.48\tau$

(*e*) $t = 0.57\tau$ (*f*) $t = 0.61\tau$

(*g*) $t = 0.70\tau$ (*h*) $t = 0.78\tau$

(*i*) $t = 0.83\tau$ (*j*) $t = 0.96\tau$

FIGURE 2. Conformation of the sunfish pectoral fin during the fin beat cycle (of period τ) in steady forward locomotion from side (left) and back (right) views. On the side views, the shading on the fin reflects distance from the body and on back views, the shades depict distance along the body.

and (iv) waves of bending that pass out along the fin. The effect of some of these fin characteristics on the thrust production will be described in detail below.

3. Computational methodology

The computational methodology employed in the current study has been described in detail by Bozkurttas *et al.* (2009). The simulations employ a sharp-interface immersed boundary method (Mittal & Iaccarino 2005) that has been described by Mittal *et al.* (2008). Here we briefly describe some of the salient features of the methodology. The equations governing this flow are the three-dimensional unsteady, viscous incompressible Navier–Stokes equations

$$\frac{\partial u_i}{\partial x_i} = 0, \tag{3.1a}$$

$$\frac{\partial u_i}{\partial t} + \frac{\partial (u_i u_j)}{\partial x_j} = -\frac{1}{\rho}\frac{\partial p}{\partial x_i} + \nu \frac{\partial}{\partial x_j}\left(\frac{\partial u_i}{\partial x_j}\right), \tag{3.1b}$$

where u_i are the velocity components, p is the pressure, and ρ and ν are the fluid density and the kinematic viscosity, respectively. These equations are discretized using a second-order, cell-centred, collocated (non-staggered) arrangement of the primitive variables (u_i, p). The equations are integrated in time using the fractional step method described by Mittal *et al.* (2008).

A multi-dimensional ghost cell methodology has been used to incorporate the effect of the immersed boundary on the flow, and this method allows us to prescribe the boundary conditions with second-order local accuracy. The fin is represented by a surface mesh with triangular elements and boundary motion is accomplished by moving the nodes of the surface triangles in a prescribed manner. Further details regarding such immersed boundary methods can be found in Ye *et al.* (1999), Udaykumar *et al.* (2001) and Mittal & Iaccarino (2005). The solver has been extensively validated by simulating flow past stationary as well as accelerating cylinders and spheres, and the accuracy of the solver for zero-thickness bodies has been demonstrated by simulating flow past a suddenly accelerated normal plate and comparing results with available experiments and simulations (Mittal *et al.* 2008).

The spanwise length of second ray, which is the longest ray of the bluegill pectoral fin, is used as the primary length scale for the current flow and is denoted by L_{fin}. The fin stroke frequency f is used as the time scale, and the mean fish velocity U_∞ is chosen to be the velocity scale. The key non-dimensional parameters for the fin are the Reynolds number (Re_f) defined as $L_{fin}U_\infty/\nu$ and the Strouhal number (St_f) defined as fL_{fin}/U_∞. Another key feature of the fin kinematics is the amplitude of the stroke that can be encapsulated in the stroke amplitude parameter defined as $A_s = D_{tip}/L_{fin}$, where D_{tip} is the maximum linear distance travelled by the tip of the second fin ray.

As pointed out before, bluegill shows little variation in the pectoral fin kinematics over a fairly large range of swimming speeds from 0.5 BL s^{-1} to about 1 BL s^{-1}. This is very important given the inherent difficulty of conducting precisely repeatable experiments with these fish. For instance, the fin kinematics described in § 2 were obtained very early on in the study, whereas the PIV data were obtained almost a year later. During this time, the fish had grown in size from about 14.5 cm to about 17.5 cm, and therefore the length velocity, and time scales of the fin stroke had changed. However, the fin kinematics and A_s remained effectively unchanged, and by making the fish swim against a current in the flume, the velocity of which can be controlled, different flapping frequencies can be elicited from the animal.

The experiments were conducted with the water channel speed set to about 1.1 BL s^{-1} and a nominal value of this speed used to determine key non-dimensional parameters was about 16 cm s^{-1}. A typical size of the fin, L_{fin}, was about 4 cm and the fish flapped its fin at a nominal frequency of about 2.17 Hz. This resulted in a fin Reynolds number of about 6300 and a fin Strouhal number of 0.54, and all

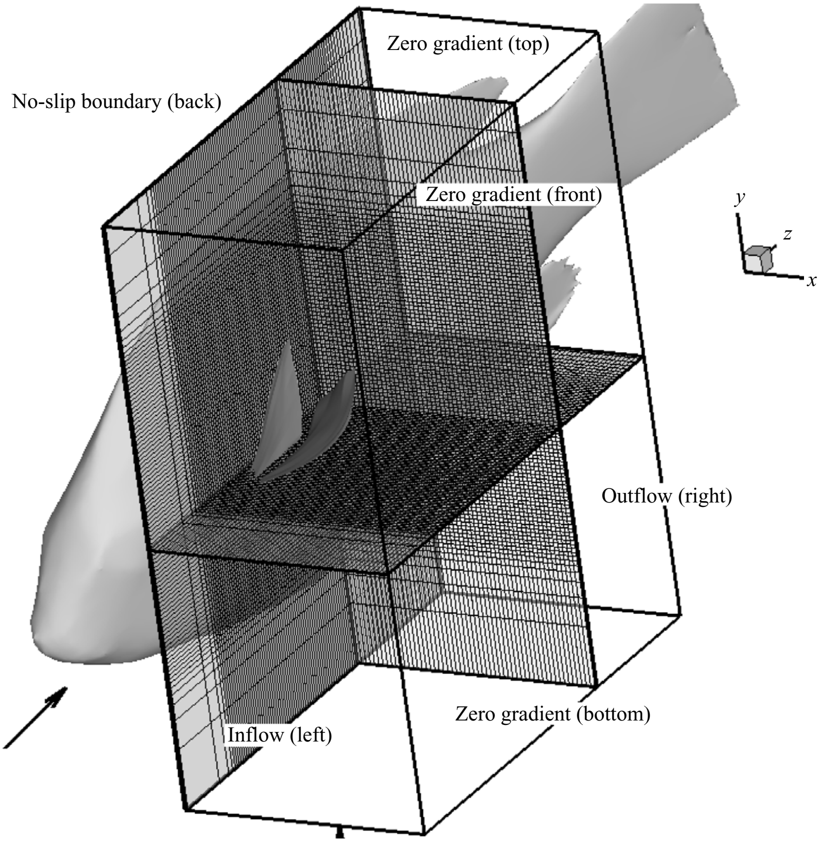

FIGURE 3. Schematic of the computational domain and grid employed in the current simulations. The figure shows two different positions of the fin during its stroke. Also indicated on the plot are the velocity boundary conditions employed at the various computational boundaries.

simulations presented in this paper have been carried out with these values of the non-dimensional parameters. Furthermore, the tip amplitude D_{tip} is about 3.4 cm, which leads to a normalized fin amplitude A_s of 0.85. All the detailed results presented in this paper are for these conditions. Matching of non-dimensional parameters and analysis of computed results in terms of non-dimensional coefficients becomes an effective tool for comparing the simulations to the experiments. However, it should be pointed out that there are always some cycle-to-cycle variation in the fin stroke even for a fish swimming in a constant velocity free stream. Variations occur in the stroke period as well as in the amplitude, and the Strouhal number probably varies by up to 10 % even during a given experiment. As shown below, despite these difficulties, effective comparisons between experiments and simulations can still be made. Note also that the Reynolds number and Strouhal numbers defined using the tip amplitude as the length scale are $Re_A \approx 5900$ and $St_A \approx 0.51$, respectively, for the current case, and these definitions sometimes make it easier to compare current results with other studies.

Figure 3 shows the computational domain used in the current study. The domain size normalized by L_{fin} is $3.8 \times 4.5 \times 1.8$. The fin is placed along one of the boundaries of the domain and a no-slip boundary condition is applied on this wall to mimic the effect of the fish body. In the lab observation, the fin is held out from the body during most of the thrust-producing periods of the stroke. Thus, the use of the above boundary condition can simplify the situation here for allowing us to incorporate the blockage effect that the fish body produces as the fin moves towards the body without having to resolve any of the flow features associated with the body. The boundary conditions used on the other boundaries are also described in figure 3. The simulations employ a large $201 \times 193 \times 129$ (4.9 million), non-uniform Cartesian grid (shown in figure 3) for the current simulations. A rectangular region around the fin and the wake is provided the highest resolution with a isotropic grid spacing of $0.012L_{fin}$ and this region has a $153 \times 159 \times 113$ (2.75 million) grid. Beyond this region of high resolution, the grid is slowly stretched out towards the outer domain boundaries. Further details regarding the choice of the grid can be found in Bozukurttas *et al.* (2009). The simulations employ a time step equivalent to $\tau/1600$ which is set by the stability requirements of the flow solver.

4. Results and discussion

Results from the current simulations are presented in this section. All the results presented here have been obtained by simulating the flow over six fin strokes. In computing mean quantities, we have discarded the first two strokes and all plots of instantaneous quantities correspond to the third cycle in the stroke by which time the flow has reached a well-established stationary state since the change of mean force coefficients in the following cycles is less than 1 %. We first discuss the hydrodynamic forces produced by the fin during the stroke, and this is followed by a description of the instantaneous vortex structures formed as well as the mean wake flow produced during the fin stroke. Following this, we present a detailed analysis of the surface traction and its connection to the vortex dynamics in order to elucidate the features of the fin and the flow mechanisms responsible for force production.

4.1. *Hydrodynamic forces*

The forces on the fin are computed through direct integration of the surface pressure and shear as described by Ghias, Mittal & Dong (2007). Since the surface of the fin is represented by triangles, we estimate the traction (pressure or shear) at the centroid of each surface triangle by using the same bi-linear interpolation that is employed for the ghost cells, and the total force on the fin is obtained by a simple trapezoidal integration scheme (Press *et al.* 2007). All the forces are presented as non-dimensional coefficients, which are computed as

$$C_F = \frac{F}{\frac{1}{2}\rho U_\infty^2 A_{fin}}, \tag{4.1}$$

where F is a generic force component and C_F is the corresponding coefficient. The total input power as shown in (1.3) is also estimated in a similar manner by surface integration of the dot product of surface traction and surface velocity associated with each triangular surface element. The three components of the force coefficients are defined as thrust (force in the $-x$ direction), denoted by C_T, lift (force in the y direction), denoted by C_L, and spanwise force coefficient (force in the z direction), denoted by C_Z.

Figure 4 shows the temporal variation of these coefficients over one cycle, and a number of observations can be made regarding these plots. First, it is noted that both

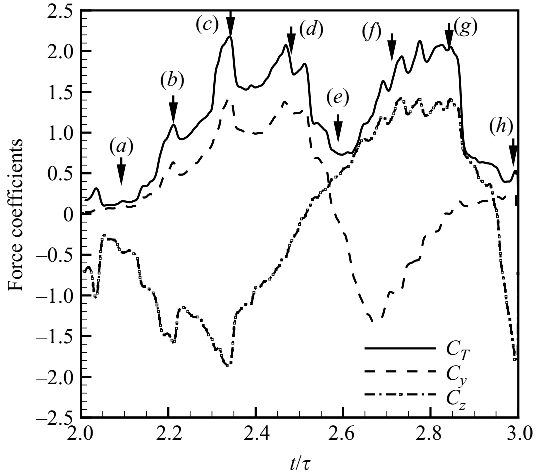

FIGURE 4. Time variation of computed force coefficients for the pectoral fin. The three-components of the force coefficients are defined as thrust (force in the $-x$ direction), denoted by C_T, lift (force in the y direction), denoted by C_L, and spanwise force coefficient (force in the z direction), denoted by C_Z.

the abduction and adduction phases of the cycle, which last from $t/\tau = 2.0$ to 2.6 and $t/\tau = 2.6$ to 3.0 respectively, produce peaks in thrust. The peak value of thrust occurs midway in the abduction part of the cycle and the value of the maximum thrust coefficient is 2.06. The peak during the adduction phase is about 2.01, which is comparable to the abduction peak. The presence of two thrust peaks during the fin stroke is confirmed by the experiments of Lauder *et al.* (2007) and Tangorra *et al.* (2008), which clearly show a forward acceleration of the fish body during both the abduction and adduction phases of the fin stroke. The estimate of thrust from measurements of the flow in a control volume around the fin also indicates peaks in thrust during both phases of the cycle (Lauder *et al.* 2007). It should also be pointed out that the shear stress on the fin contributes a drag which is less than 10 % of the pressure thrust magnitude (Bozukurttas *et al.* 2009), and is therefore dynamically insignificant.

It is also interesting to note that whereas the minimum thrust is produced during the start and completion of the stroke, the fin produces positive thrust during all phases in its stroke. This is in contrast to all of the rigid flapping foils studied so far which usually produce drag at the top and bottom portions of the flapping cycle. For instance, experimental measurements of a foil undergoing a combined pitching–rolling motion produced a drag force at the top and bottom of the stroke (Techet *et al.* 2005). Similarly, a thin ellipsoidal foil, with an aspect ratio of 2.55 undergoing a pitching–heaving motion studied by Dong *et al.* (2006), produced a peak drag coefficient of about 0.3 during the two ends of the stroke. This was a significant fraction of the peak thrust, which was about 0.7. The ability of the fin to produce positive thrust, especially during the abduction part of the cycle where the fin moves out and against the incoming flow, is particularly remarkable and it is not clear at the outset as to what are the flow mechanisms responsible for this. Below, we will focus on this aspect and provide a better understanding of this behaviour.

The mean and minimum-to-maximum (min–max) variation for the three force components obtained from the current simulation, available data from the companion

Study ↓	Quantity →	C_T	C_L	C_z	Remarks
Current	Mean	1.18	0.22	−0.16	Bluegill fin
	Min–max	2.1	2.6	3.1	$St=0.54$, $Re=6300$ ($St_A=0.51$, $\mathrm{Re}_A = 5900$)
Lauder *et al.* (2007); PIV	Min–max	2.4	2.7	3.7	Bluegill fin
(body acceleration based)	Min–max	2.1	2.2	–	$St=0.54$, $Re=6300$
Mittal *et al.* (2006)	Mean	1.05	0.25	−0.21	Bluegill fin
	Min–max	2.05	2.4	2.95	$St=0.54$, $Re=1440$
Dong *et al.* (2006)	Mean	0.246	0	0	Rigid pitching–heaving foil
	Min–max	1.05	4.8	0	$St_A=0.6$, $Re=200$
Techet *et al.* (2005)	Mean	≈0.4N	–	–	Rigid pitching–rolling foil
	Min–max	≈1.2N	≈6.1N	–	$St_A=0.29$, $Re\approx 5\times 10^4$

TABLE 1. Mean and variation of hydrodynamic forces computed for the current fin compared with previous computational as well as experimental studies.

experiments (Lauder *et al.* 2006, 2007), as well as data from some selected rigid flapping foil studies are presented in table 1, and a number of interesting observations can be made from this table. First, the mean values of the lift and spanwise forces produced by the fin are quite small compared with the mean thrust. From a hydrodynamic point of view, this is surprising since the fin motion during abduction is very different from that during adduction, but despite this, the lateral (vertical or spanwise) forces during these two phases of the stroke nearly balance out. From an organismal point of view, this is quite understandable since it stands to reason that during steady forward swimming, the fish will adopt a fin gait that minimizes any lateral drift. Experimental visualizations (Lauder *et al.* 2006, 2007) also indicate very little vertical drift in the location of the fish body, which tends to corroborate the current observations.

The min–max variations of the computed forces are also provided in table 1, and these can be compared with the corresponding experimental results provided by Lauder *et al.* (2007). In their experiments, Lauder *et al.* (2007) have estimated the forces produced by the fin using two methods. In the first method, they have measured all three components of velocity on a rectangular streamwise plane located in the wake of the fin (denoted by $x_1=X$) using PIV. The force imparted by the fin on the fluid can then be estimated by using a control-volume analysis and evaluating the momentum flux through this plane as follows:

$$F_i(t)=\rho\int_{x_2}\int_{x_3} u_1(X,x_2,x_3,t)\,u_i(X,x_2,x_3,t)\,\mathrm{d}x_2\,\mathrm{d}x_3. \tag{4.2}$$

There are a number of assumptions inherent in the above PIV-based, control-volume estimate (see for instance Dabiri 2005 for a discussion on this), the major ones being that the pressure is assumed to have recovered to the free-stream value at this plane and that the boundary layer on the body of the fish does not influence the wake of the fin at the location where the measurements are taken.

In the second method, Lauder *et al.* (2007) have used high-speed, high-resolution visualization to track a point on the body of the fish that is close to the centre of mass of the fish. By differentiating the location of this point twice in time and knowing the mass of the fish, the time variation of the streamwise and vertical force on the body of the fish can be estimated. Note that this technique provides the *total* forces on the fish, which include the drag force on the fish body and the vertical force due to gravity (buoyancy minus weight) on the fish. Thus, the mean forces produced by the fin cannot be easily extracted using this method. However, given that both the drag and force due to gravity are expected to be nearly constant, the min–max variation of the forces estimated using this method should be a close approximation of the min–max forces produced by the fin. Note also that since the fish strokes both of its pectoral fins symmetrically, the net spanwise acceleration of the fish at all time instants is nearly zero and, therefore, this second method does not provide any estimate of this component of force. Table 1 shows that there are indeed some differences between the min–max forces estimated from the two methods. In particular, the PIV-based estimate is higher than the body-acceleration-based value for both force coefficients, with the PIV-based value of min–max lift force being almost 23 % higher than the corresponding value obtained from the body acceleration. Nevertheless, the two methods, when taken together, do provide us with a fairly reasonable estimate of the force components.

We now compare the computationally determined force coefficients with ones estimated in the experiments. However, in addition to the limitations of the experimental measurements described above, there are a few other factors that add to the uncertainties that are inherent in comparing the computational results to the experiments. Chief among these is the inability to ensure a precise match between the kinematics used in the computation and the kinematics employed by the fish during the experimental measurements. This is primarily due to the limitations of the experiments; the fin kinematics and the forces produced by the fin (both using PIV and through body acceleration) were not obtained simultaneously. Consequently, there is always some level of variation in the fin kinematics from stroke to stroke. Thus, it is not possible to ensure that the fin kinematics employed in the CFD analysis are *precisely* the same as the ones for which the force data are estimated in the experiments. This could potentially contribute to some variability between the experimental and computational forces.

Table 1 shows that the computed min–max forces produced by the fin are consistently lower than the PIV-based experimental values by up to 16 %. However, the relative magnitude is very well predicted. Both the computations and experiment show that the min–max variation in the thrust force is the lowest and that variation in the spanwise force is roughly about 50 % higher than that for the thrust force. The variation of the lift force is intermediate between these two force components in both the simulations and experiments. Note that the min–max value of the thrust coefficient predicted from CFD matches that obtained from the body acceleration quite well, and the corresponding value for the vertical force lies between the two experimental estimates.

The comparison of the mean values is complicated by the fact that the mean values of the forces have a lower magnitude and are therefore subject to a larger relative uncertainty in the experimental estimates. This is especially true for the vertical and spanwise components, which are very small, but even the mean thrust is about half the min–max value. Furthermore, measurements of momentum flux in the wake of the fin might get affected by the boundary layer on the body of the fin, and this can alter the mean thrust force estimate of the fin. We have, therefore, adopted another approach that allows us to assess the computed mean thrust against experiments by noting that for steady-state forward swimming, the mean thrust produced by the fish is balanced out by the drag produced by the rest of the body. Drucker & Lauder (2000) have estimated the drag force on a bluegill sunfish with lengths of

20.3 ± 0.9 cm swimming at $0.5\,\mathrm{BL\,s^{-1}}$ to be $10.6 \pm 0.5 \times 10^{-3}$ N. Assuming that the coefficient of drag for these species of fish is constant and that the frontal area of the fish is proportional to the square of the length of the fish, we can rescale the drag force for the current fish, and this gives us a drag value of $28.3 \pm 6.2 \times 10^{-3}$ N. If we take half of this force (with the assumption that the two pectoral fins produce equal thrust to counter the total drag on the body), and non-dimensionalize it as in (4.1), we get a fin thrust coefficient of 1.03 ± 0.23. The value of 1.18 predicted from CFD is, therefore, found to fall within the range estimated from the experiments. It should, however, be noted that there are potentially, significant sources of uncertainly inherent in our estimation of experimental drag. These include the uncertainty in the experimental measurement as well as our assumption that the drag coefficients at two significantly different swimming speeds for two different fish specimens are equal. However, the fact that we also match the peak-to-peak values of the experiments quite well indicates that uncertainties in the modelling and experimental are reasonable. Thus, the force coefficients obtained from the computations are in good agreement with the experiments, and these along with the grid refinement and domain-size studies give us a high level of confidence in the fidelity of the computational modelling.

In the table we also provide the mean and min–max values for previous simulations for this pectoral fin at a Reynolds number of 1440 and $St = 0.54$, which was described by Mittal *et al.* (2006). This simulation was carried out for the same kinematics; however, the Reynolds number was limited to a value that was about four times lower than the actual value due to CPU time limitations. A comparison shows that both the mean and the min–max values compare well with this lower Reynolds number simulation, therefore indicating that the fin performance is relatively insensitive to the Reynolds number. The effect of the Reynolds and Strouhal numbers on the fin performance and hydrodynamics has been examined more thoroughly by Bozukurttas *et al.* (2009).

A comparison of these min–max variations with past studies on rigid foils leads to some additional interesting insights. A good measure of the oscillatory nature of the forces produced by the fin is the ratio of the vertical min–max force to the mean thrust force. For the bluegill, this value is $2.6/1.18 = 2.20$. Although it is difficult to precisely match the operational parameters between the fish fin and engineered rigid foils, it is nevertheless useful to make comparisons with available data on engineered flapping foils. There are a number of studies that have examined flapping foils in the past (see Mittal 2004) but we limit the comparison to finite-aspect ratio foils since these are geometrically and kinematically closer to the current case. For instance, Dong *et al.* (2006) have used numerical simulations to examine the fluid dynamics and thrust production of finite-aspect ratio rigid flapping foils. These foils underwent a combined, sinusoidal pitching and heaving in the vertical plane. Reynolds numbers (defined as $U_\infty c/\nu$, where c is the foil chord) in this study varied from 100 to 400, and the Strouhal number (defined as fA/U_∞, where f is the flapping frequency and A is the total flapping amplitude) also varied over a large range from 0.4 to 1.2. Considering the results for a foil with aspect ratio of 2.55 and $St = 0.6$, which is similar to that of pectoral fins, it is found that the min–max variation of the lift force (table 1) is 19.5 times the mean value of thrust.

Another study of particular note in the current context is that of Techet *et al.* (2005), who examined the force and efficiency of a flapping foil with aspect ratio (span/chord) of about 4.5. The chord-based Reynolds number (Re) in these experiments was about 5×10^4, the Strouhal number based on tip amplitude (St_A) varied from 0.29 to 0.86, and tip amplitude normalized by chord (A_s) varied from 1.4 to 2.8. Note that the current values for the fish fin are $Re = 6300$, $St_A \approx 0.51$ and $A_s \approx 0.85$. Estimates of forces have been obtained from the plots in this paper, and these estimated values are included in table 1 (Techet *et al.* 2005). For the case with $St_A = 0.29$ and $A_s = 2.14$ for which plots are provided in this paper, estimates indicate that the min–max variation in the lift force is about 15 times the mean thrust. Thus, the two extreme cases described above (two-dimensional, low Reynolds number foil in simulation and three-dimensional, high Reynolds number case in the experiment) indicate that in contrast to the fish fin under study here, rigid flapping foils usually produce instantaneous lateral forces that are significantly larger than the corresponding thrust force. This has a number of interesting and important implications which are discussed below.

First, it should be noted that at the steady forward speed at which this study has been conducted, the fish uses a symmetric stroke for the two pectoral fins, i.e. both pectoral fins abduct and adduct at the same time. Thus, whereas symmetric stroking effectively cancels out, the instantaneous and net spanwise force on the fish, the lift forces contributions from the two fins add up at any time instant. Thus, a reduction in the instantaneous level of vertical fin force directly translates into a reduced heaving oscillation for the fish body. Given that stabilization of the visual field is an important characteristic that animals strive for (Milne & Milne 1965; Kern & Varju 1998), it is quite reasonable to hypothesize that the fin gait is designed in part to produce reduced body oscillations, thereby leading to a more stable visual field.

Second, it should be pointed out that the sunfish, like many other fish species, is transversely unstable, i.e. its centre of buoyancy is below its centre of gravity (Drucker & Lauder 2002). Thus, the fish not only has to produce thrust force with its pectoral fins but also has to constantly produce restoring moments to avoid an unstable roll. With this highly unstable equilibrium situation, it is likely that the fish tries to minimize body oscillations resulting from the pectoral fin motion, and this would be another factor that would drive a force production profile that keeps oscillatory transverse forces to a minimum. Third, a lower min–max variation in the forces about their mean values also implies a reduced level of the maximum bending moments experienced by the fin rays at their roots. This is likely also important for the fish since high levels of instantaneous bending moments could damage the fin rays, which would have serious consequences for the animal.

Finally, as apparent from the expression for propulsive efficiency in (1.4) and (1.6), large lateral forces combined with lateral fin velocity are the primary constituents of the parasitic power expended by the fin. Thus, large lateral forces are one factor that can result in reduced propulsive efficiency. In fact, the computation of the propulsive efficiency through the formula shown in (1.6) of the pectoral fin indicates a value of 0.60 (or 60 %). Note that, to our knowledge, this is the first time that a value of propulsive efficiency has been obtained for the fin of a fish during natural swimming by direct computation of power from surface forces and velocities.

How well does this efficiency compare with that of engineered flapping foils? Here again, we make comparisons with the results obtained by Techet *et al.* (2005). From the large sequence of test cases that they have studied, we choose a case that best matches our parameters. The lowest amplitude case studied by Techet *et al.* (2005) has $A_s = 1.4$, which is about 50 % higher than the current case. For this case, a peak efficiency for $St_A \approx 0.50$ is estimated from their graphs to be about 63 %, which is comparable to the current case. It is interesting to note that the thrust coefficient for this case (the thrust coefficient in this study is defined in a manner similar to ours, so a direct comparison can be made) is estimated to be 0.62, which is lower than the current value of 1.09. Another way to compare the performance of the fish fin with the engineered foil is to note that among all of the 60 cases presented by Techet *et al.* (2005), the highest thrust coefficient obtained for any foil with an efficiency greater that 60 % (it is 61.4 % for this case) is 1.26 and this occurs for $St_A = 0.71$ and $A_s = 2.14$. It should be noted that the fin Reynolds number is also an order of magnitude lower than this rigid foil, and thus the shear drag that the fish fin has to overcome is also expected to be higher than the rigid flapping foil (Bozukurttas *et al.* 2009).

Thus, in summary, the fish fin produces a combination of thrust and efficiency that is comparable to the best performing rigid flapping foil, and it does this at lower Strouhal and Reynolds numbers and at a much lower normalized amplitude compared with the rigid foil. This high level of propulsive performance is obtained without producing large instantaneous levels of lateral forces, consequently allowing the fish to propel itself forward in a stable manner with very low levels of body oscillations. In contrast to engineered flapping foils, which are made of hard materials such as metal/composites and which have strong (and heavy) linkages able to withstand large torques, the fish fin produces efficient propulsion with a very thin, lightweight and flexible fin that does not have to contend with large bending moments.

5. Vortex topology

The wake vortex topology of flapping foils has received considerable attention in literature (Koochesfahani 1989; Triantafyllou, Hover & Licht 2003; Dong *et al.* 2006). It has been shown that for two-dimensional foils undergoing a combined pitching–heaving motion, the highest propulsive efficiency is attained at Stouhal numbers (defined as $St_A = fA/U_\infty$, where A is the total amplitude) between about 0.25 and 0.35 (Triantafyllou *et al.* 2003). Furthermore, this optimal thrust condition coincides with the formation of a well-organized inverse Kármán vortex street. The inverse Kármán vortex street is most effective in producing a compact, directed jet and is, therefore, the optimal wake topology. Furthermore, the vortex street is the result of a convective instability of the mean jet profile, which has a maximum spatial growth in the Strouhal number range mentioned above. Hence the above Strouhal number range results in optimal efficiency. Observation and measurements for freely swimming fish and cetaceans that swim using caudal (tail) fin propulsion have indicated that these animals swim so that their Strouhal numbers are roughly in this optimal range (Triantafyllou *et al.* 2003). This provided some verification that the optimal condition found via theory and simple experiments also extends to more realistic settings.

The recent studies of Blondeaux *et al.* (2005), Buchholz & Smits (2006) and Dong *et al.* (2006) have addressed the wake topology of finite-aspect ratio flapping foils. In Dong *et al.* (2006), the hydrodynamics of foils with aspect ratios ranging from 1.27 to 5.09 were examined, and the key conclusion was that the wake topology of these finite-aspect ratio flapping foils did not exhibit the inverse Kármán vortex street. Instead, the wake was dominated by two sets of counter-rotating vortex rings (or loops) that convected on either side of the wake centreline along oblique directions. This resulted in a mean wake that was composed of two oblique jets. Thus, observations made for two-dimensional flapping foils do not simply carry over to lower aspect-ratio three-dimensional flapping foils. Given that the fish fin represents a significantly more complex situation than the rigid flapping foils that have been studied before (due to the complex kinematics, deformation and planform associated with the fish fin), it is expected that the vortex topology associated with the fin will also be more complex.

The companion experimental studies of Lauder *et al.* (2006, 2007) have used dye visualization to show the presence of a distinct leading-edge vortex on the dorsal

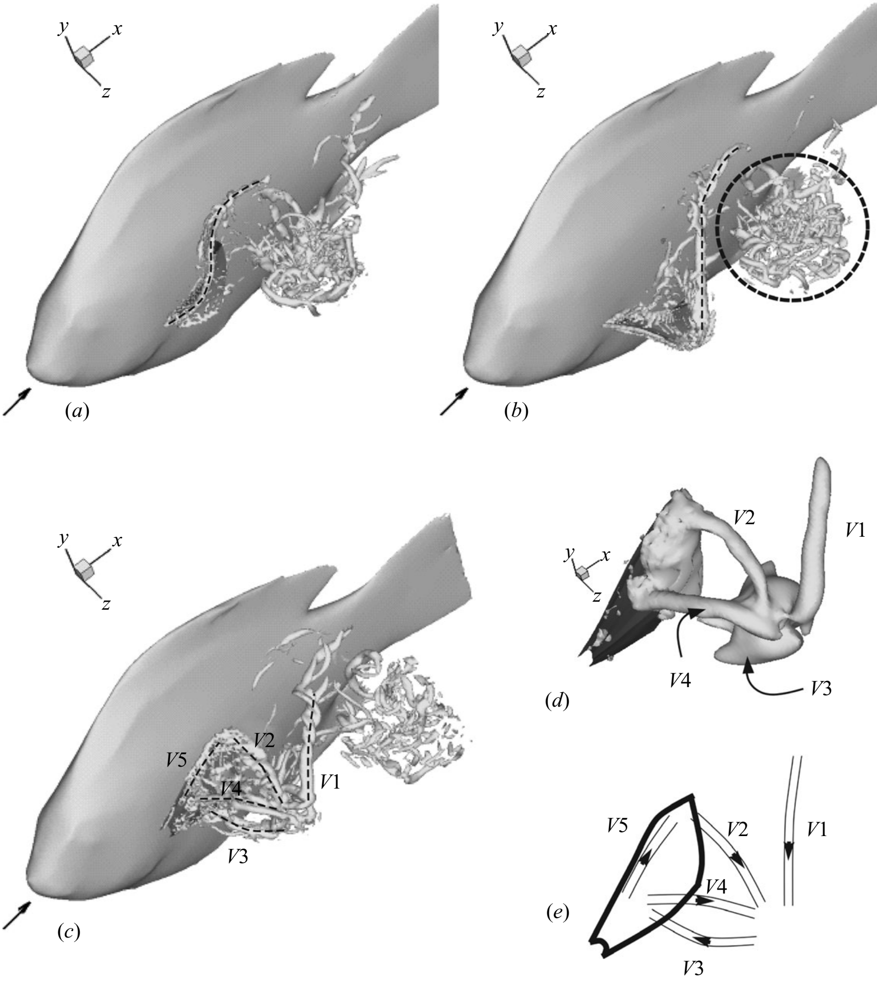

FIGURE 5. Vortex structures formed by the fin motion at various stages in the fin stroke. (*a*) $t/\tau = 1/3$, (*b*) $t/\tau = 2/3$, (*c*) $t/\tau = 1$. (*d*) Isosurface of pressure corresponding to a non-dimensional value of -0.25 at $t/\tau = 1$. Regions of low pressure clearly identify all of the key vortices in the flow at this instant. (*e*) Schematic of the five distinct vortices that are observed at the end of the stroke ($t/\tau = 1$). $V1$ and $V2$ are the abduction and adduction tip vortices, respectively; $V3$ and $V4$ are the vortices shed from the ventral and dorsal leading edges, respectively, during the early stage in adduction; and $V5$ is an attached leading-edge vortex during the later stages of adduction. The arrows denote the direction of rotation for the vortices according to the right-hand-side rule.

edge of the fin during abduction. PIV measurements at selected planes also indicate that the wake of the fin has a highly complex structure. One of the objectives of the current simulations, therefore, is to augment these experimental observations by providing a more detailed and comprehensive view of the vortex topology over the fin as well as in the wake.

Figure 5 shows the vortex structures produced by the fin at three different instants in the fin stroke. The vortex structures are identified by plotting the isosurface of the magnitude of the imaginary part of the complex eigenvalue of the velocity deformation tensor (Soria & Cantwell 1993; Mittal *et al.* 2006). The isosurface plotted here corresponds to a magnitude of 1.2 and is chosen so as to clearly show the significant vortical structures. Figure 5(*a*) shows the vortex structures at an early stage ($t/\tau = 1/3$) of the fin stroke, and the key vortex structure (identified by a dashed line) that is observed is a compact dorsal leading-edge vortex. The vortex is located on the posterior surface of the fin and extends from the root of the fin out past the fin tip into a tip vortex. Also visible is a conglomeration of vortex structures in the near wake that were produced by the previous fin stroke.

Figure 5(*b*) shows the vortex structures at $t/\tau = 2/3$, which is after the fin has initiated the adduction phase. One of the most visible vortex structures at this phase is the strong tip vortex (identified by a dashed line) that extends from the tip of the fin all the way into the wake over a distance that is roughly twice the size of the fin. Also visible is the dorsal leading-edge vortex on the anterior surface of the fin (highlighted by an arrow) that is formed due to the rapid backward motion of the fin during adduction. The vortex conglomeration associated with the previous fin stroke (identified by a dashed circle) maintains its compact nature but has convected farther downstream.

Figure 5(*c*) shows the vortex structures at $t/\tau = 1$, which represents the completion of the fin stroke and a number of distinct vortex structures are observed at this phase of the cycle. The tip vortex formed during the abduction phase (denoted by $V1$ in the figure) is now completely separated from the fin and extends far into the wake. Interestingly, this tip vortex can be observed to be formed of helical vortex filaments which are reminiscent of the tip vortex structure of a lifting wing (Dyke 1982). Also visible is another tip vortex (identified as $V2$), which is formed due to the fin adduction. There are also two vortices ($V3$ and $V4$) that can be identified, and these are leading-edge vortices shed by the ventral and dorsal leading edges, respectively. Note that in this context no such separated leading-edge vortices are observed during the abduction stage, indicating that the dorsal leading-edge vortex identified in figure 5(*a*) remains attached to the leading edge throughout the abduction stroke. We will discuss this issue in the next section, where we discuss the thrust production mechanisms. Finally, at this phase, we also identify an attached dorsal leading-edge vortex ($V5$), which is formed after the LE vortex ($V4$) formed earlier in the adduction phase has shed from the leading edge.

Plotted in figure 5(*d*) is one isosurface of the pressure corresponding to a non-dimensional pressure value of -0.25 at $t/\tau = 1$. This plot shows the correlation between identifiable vortex structures and regions of low pressure. Vortices $V1$–$V4$ can be clearly identified in this plot, whereas vortex $V5$ is buried inside a low-pressure region on the fin surface. Also noticeable in this plot is a large region of low pressure at the intersection of the four vortices $V1$–$V4$. Finally, in figure 5(*e*), we attempt to clearly delineate the location and shape of these vortices by drawing a ‘skeleton’ of the identifiable vortex structures at the end of the stroke.

Thus, at the end of the stroke, there are a number of distinct and strong vortex structures that are created and released by the fin. Given the tight proximity of these vortex structures, they are subject to mutual induction effects as they convect downstream. These induction effects lead to deformation (stretching and turning) of the vortex filaments, and it is these induction effects that result in the highly complex conglomeration of vortices that are observed in the wake.

6. Thrust production mechanisms

In the previous sections we have described the thrust production of the fin as well as the vortex dynamics. The fin produces high levels of thrust and does so with a relatively high propulsive efficiency. Furthermore, this high level of propulsive performance is obtained with a Strouhal number and amplitude that is lower than that employed by typical rigid foils. The underlying mechanisms are clearly connected with the ability of the fin to deform both along the chord and the streamwise direction. Earlier studies of rigid flapping foils (Ellington *et al.* 1996; Anderson *et al.* 1998) have indicated the importance of the leading-edge vortices in the production of thrust. The current fin motion and geometry is, however, significantly more complicated than these canonically engineered flapping foils and, as has been described in the previous section, the flow past the fin is dominated by more than one distinct and strong vortex structures. Thus, a detailed analysis is needed in order to gain insight into the connection between the fin kinematics, vortex dynamics and force production, and that is what we attempt to do in the current section.

6.1. *Vortex dynamics and surface force distribution*

The analysis described in this section is based on figure 6. In this figure, we have shown the fin at eight phases in the fin stroke. These eight phases are indicated in the thrust coefficient plot in figure 4 and are chosen at a key point where the thrust variation shows distinctive behaviour (such as a local maximum or minimum). For each phase, we show two plots in figure 6. The plot on the left-hand side shows a close-up view of the vortex structures. The right-hand-side plot shows contours on the surface of the fin that correspond to the local thrust force due to pressure (which is normal to the fin surface) experienced by each of the surface triangles. The colour scheme for these surface contours is such that blue colours represent the highest thrust force. Also plotted are vectors on the surface that denote the direction and magnitude of the force experienced locally by the fin.

Figure 6(*a*) shows the vortex structure and surface force at $t/\tau = 0.10$, which is the early stage of the abduction phase. It should be noted from figure 4 that the fin produces a small positive thrust at this time instant. The vortex structure shows that even at this early stage, there is a leading-edge vortex that is formed at the dorsal leading edge and the surface contour plot also shows that it is precisely in this leading-edge region that the small amount of thrust is generated. In figure 6(*b*), at the phase of $t/\tau = 0.22$ the fin has progressed farther in its abduction phase, and it is observed that the dorsal leading-edge vortex now extends into a tip vortex. The force vectors indicate that the surface force magnitude has increased from the previous phase. Furthermore, the entire dorsal leading edge (from root to tip) produces nearly an equal magnitude of surface force, and this is clearly associated with the nearly uniform dorsal leading-edge vortex. However, surface contours of the local thrust force show that the thrust is mostly created near the spanwise tip, and this is primarily because only near the tip is the surface orientation such that it has a forward projection.

The next phase of $t/\tau = 0.34$ is shown in figure 6(*c*), and the first major peak in thrust is attained at this phase. As can be seen, the fin orientation and shape at this phase is significantly different from the previous phase. In particular, we observe a significant chordwise surface curvature (a ‘cupping’ of the fin) and, at the same time, we also notice a significant spanwise curvature in the dorsal leading edge. Whereas the former (chordwise curvature) is actively controlled by the fish through its control of the individual fin rays, the latter (spanwise bending) is mostly a result of the hydrodynamic loading of the fin. The larger magnitudes of the surface force are now located in the outer half of the fin, and the chordwise curvature essentially allows the dorsal leading edge to supinate so as to reorient this surface force in the direction of thrust.

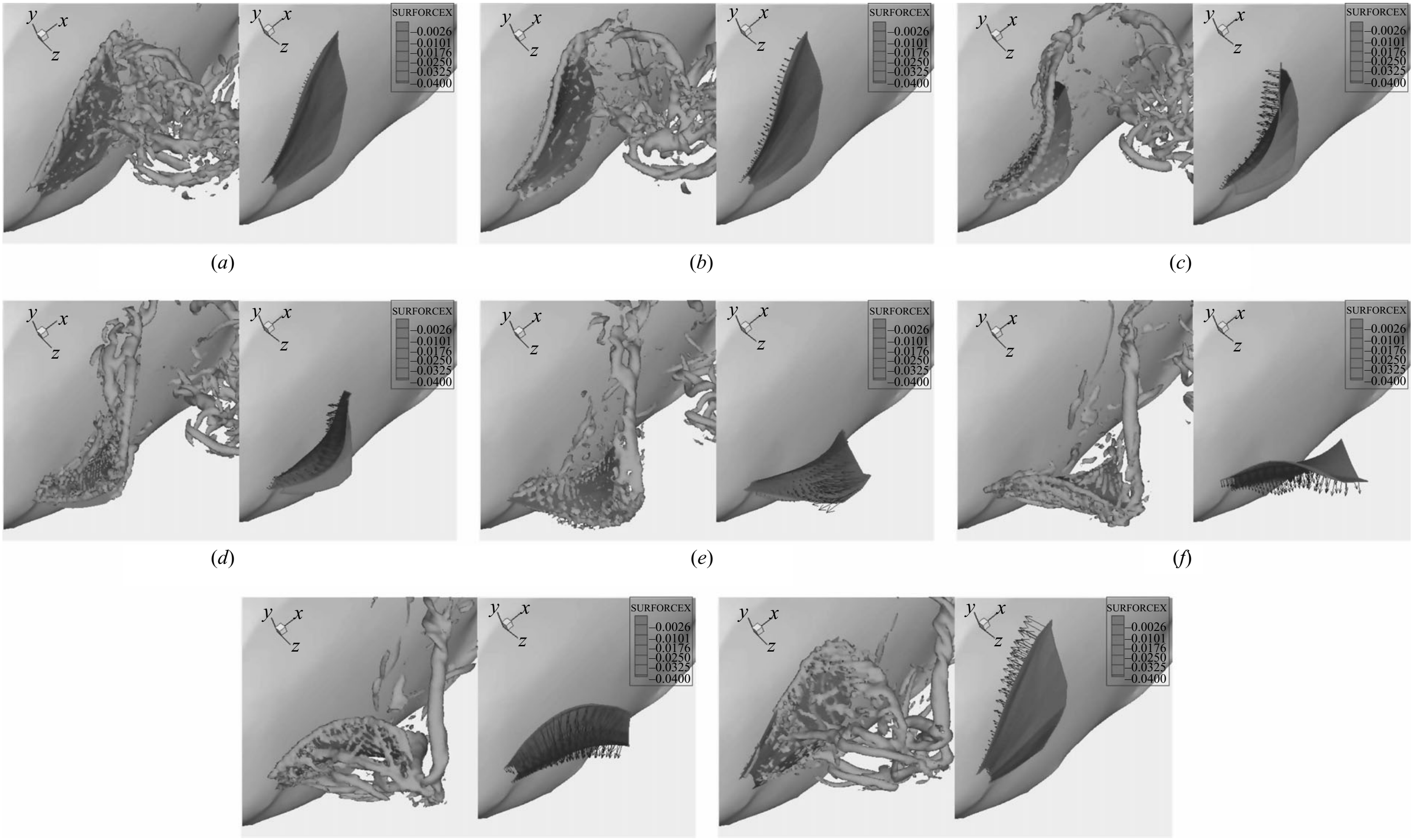

(*a*) (*b*) (*c*) (*d*) (*e*) (*f*) (*g*) (*h*)

FIGURE 6. Vortex structures and surface force at selected phases in the fin stroke. The vortex structures are identified using the same criterion as for figure 5. The contours on the fin surface show the non-dimensional surface force per unit area along the x (flow) direction with negative values indicating a positive thrust force. The arrows on the fin surface indicate the local surface traction which shows the direction and magnitude of the instantaneous hydrodynamic force exerted on the fin. (*a*) $t/\tau = 0.1$, (*b*) 0.22, (*c*) 0.34, (*d*) 0.48, (*e*) 0.59, (*f*) 0.72, (*g*) 0.84, (*h*) 1.0.

The next phase of $t/\tau = 0.48$ shown in figure 6(*d*) corresponds to another significant thrust peak in the abduction phase. At this phase, we see a strong tip vortex extending from the fin tip into the wake. Interestingly, the surface force vectors at this phase are slightly smaller in size compared with those of the previous phase. Furthermore, this surface force is now even more distinctly limited to the spanwise tip region, and the region of the dorsal leading edge near the root of the fin produces almost no force. This is clearly due to the fact that at this phase, the velocity of the dorsal leading edge is quite small. Interestingly, despite the overall lower magnitude of surface force on the fin at this phase, the force coefficient in figure 4 indicates that the overall thrust produced is quite comparable to the previous phase. The primary reason for this is the increased chordwise curvature that has further tilted the surface force vector in the thrust direction. Thus, whereas the thrust peak at the previous phase is associated with large magnitudes of surface force, the current thrust peak produced due to the tilting of the surface force in the thrust direction.

Figure 6(*e*) corresponds to $t/\tau = 0.59$, which is nearly at the end of the adduction phase. The force coefficient plot in figure 4 indicates a local minimum at this phase. Note, however, that even at this phase in which the fin is transitioned from abduction to adduction, the thrust force is fairly significant. From a kinematic point of view, this is due to spanwise flexibility of the fin, which results in a wave propagating from the root to the tip of the fin. Consequently, even though the dorsal leading edge near the fin root has already initiated adduction, the outer portion of the fin is still undergoing abduction and is still able to produce thrust force. The hydrodynamic consequence of this is clear in figure 6(*e*), where at the spanwise tip there exists a strong tip vortex that produces most of the thrust force (as seen by the surface contours).

The next phase shown in figure 6(*f*) is at $t/\tau = 0.72$, which is early in the fin adduction stage. Note that by the end of the abduction phase, the ventral portion of the fin has also moved in such a way that the fin is no longer 'cupped'. During the adduction stage, the entire fin moves backward towards the body in a coordinated manner similar to a paddle moving in the water during its power stroke (Walker & Westneat 2000). The result, as we see from figures 6(*f*) and 6(*g*), is that the surface force is more uniformly distributed over the fin. However, given that the speed of the tip is always the highest and also given the orientation of the tip region of the fin, we find that even during the adduction phase, the tip region of the fin produces most of the thrust. Also noticeable are the series of leading-edge vortices that are shed from the dorsal leading edge due to the rapid backward motion of the fin. The net result of this is that even during adduction, the fin produces a thrust magnitude similar to that produced during the abduction stage. This is quite remarkable since the motion and the underlying hydrodynamic mechanisms employed in these two phases are very different.

Dong *et al.* (2006) have shown that finite-aspect ratio flapping foils produce highly divergent wakes due to mutual vortex induction mechanisms. In particular, the wakes are characterized by two divergent jets that are at significant angles to the wake centreline. In direct contrast to the narrow, intense jets that are characteristic of high propulsive performance, wide divergent jets indicate low levels of thrust and efficiency. It is, therefore, of interest to examine the mean wake created by the fish fin, and in figure 7(*a*) we show one isosurface of the mean streamwise velocity (corresponding to $1.24U_\infty$). The jet does not seem to show any significant lateral expansion and remains fairly compact. Figure 7(*b*) shows contours of mean streamwise velocity on one streamwise plane (plane indicated in figure 7*a*). This plot shows that peak mean values in the wake are about 30 % higher than those in the free stream. Furthermore,

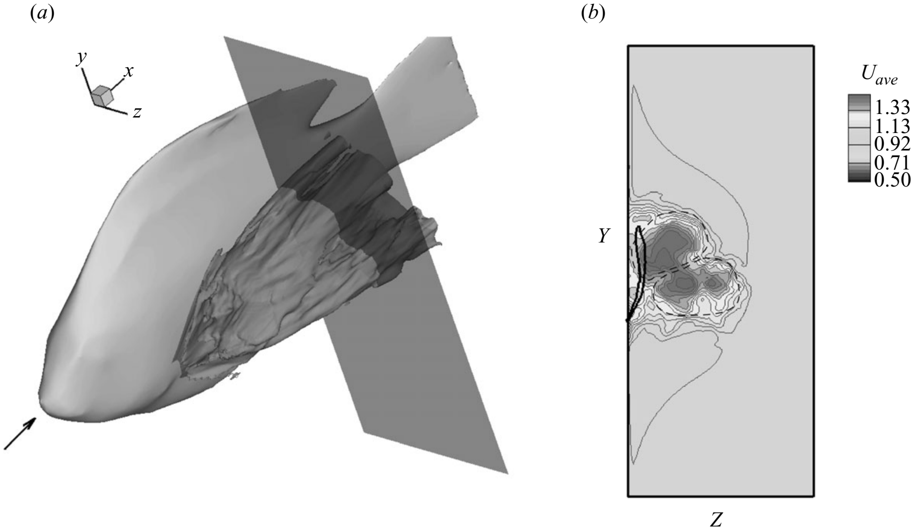

FIGURE 7. Mean topology of the wake of the fin. (*a*) Three-dimensional view of one isosurface of the mean streamwise velocity corresponding to a value of $1.24U_\infty$ and (*b*) contours of the mean streamwise velocity on the streamwise plane shown in (*a*). The two dashed ovals in (*b*) delineate two regions of concentrated streamwise momentum excess in the wake of the fin.

it seems that similar to the wake of a rigid flapping foil, the wake of the fin has two regions (indicated by dashed lines) of concentrated streamwise momentum. Thus, while there is some topological similarity between fin and flapping foil wakes, the wake of the fin is more compact. This is a further sign of the higher propulsive performance of the bluegill fish fin.

6.2. *Significance of fin tip kinematics*

The dominance of the fin tip region in the thrust production is further established by plotting contours of the time mean local thrust force in figure 6. These plots clearly show that a small region near the dorsal fin tip is responsible for producing most of the thrust. It is, therefore, useful to examine the motion of the tip in detail, especially over the abduction phase since the fin tip undergoes a fairly complex motion during this phase and produces a thrust distribution that is significantly focused on this region. In figure 8, we plot three views of the motion of the fin. In all of the views, we have tracked and identified (with a solid black line) the outermost (towards the tip) portion of the dorsal leading edge. Figure 8(*a*), which is the front view, shows the motion of the fin tip in a plane lateral to the flow. It is, however, the two other views that prove more illuminating. Figure 8(*b*) shows the top view, where the flow direction is from the bottom to top. In this view it becomes readily apparent that the dorsal fin tip is undergoing a motion that closely resembles a combined pitching–heaving motion in the spanwise direction. This spanwise pitching–heaving motion is initiated as soon as the fin starts to abduct and is partially responsible for the early establishment of thrust over the fin.

Now we turn our attention to the side view in figure 8(*c*), where the flow direction is from left to right. The first thing we note in this view is that the fin tip first undergoes an upward motion as the fin expands and the dorsal leading edge extends into the flow. Then, as the fin starts to 'cup', the fin tip rapidly moved downward. What becomes apparent in this view is that the motion that the fin tip undergoes (fin

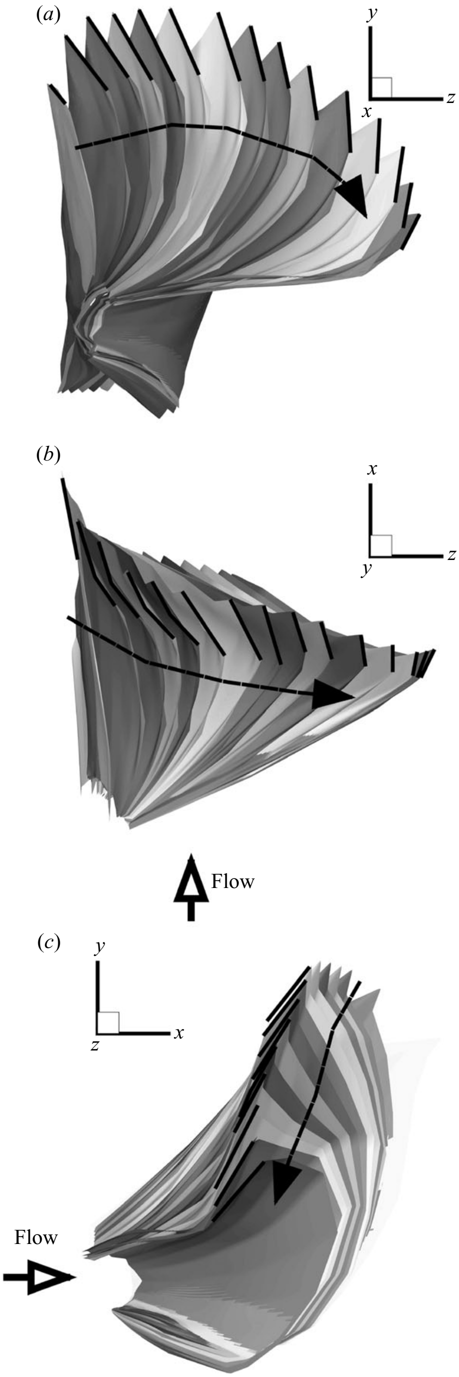

FIGURE 8. Three views of the fin motion during abduction with the trajectory of fin tip identified using a black line segment. (*a*) Front view; (*b*) top view; (*c*) side view. Both the top and side views clearly show that the fin tip undergoes a pitching–heaving (or ‘flapping’) motion in the spanwise as well as in the dorso-ventral direction.

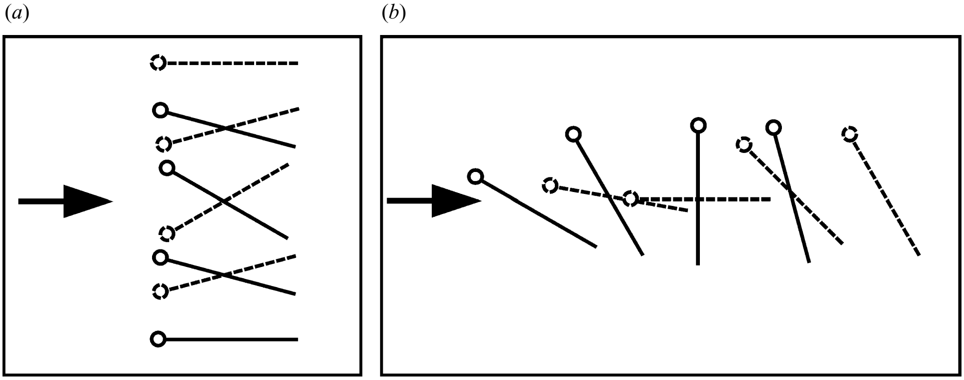

Figure 9. (*a*) Typical pitching–heaving (flapping) kinematics with upstroke and downstroke denoted by solid and dashed lines, respectively. (*b*) Typical 'paddling' kinematics with backstroke and forward strokes denoted by solid and dashed lines, respectively. Direction of flow relative to body is shown by the large arrow.

tip is marked by black line segments) is also that of a combined pitch-and-heave in the vertical direction.

Thus, the remarkable conclusion is that the fish employs both active and passive fin deformation to produce kinematics of the fin tip during abduction that is effectively a pitching–heaving in both spanwise and vertical directions. Note that the fin tip is *the* region of the fin that has the fastest velocity, and since hydrodynamic forces nominally scale with the square of the velocity, the kinematics of the fin tip are critical to force production. The spanwise pitching–heaving action is activated at an early stage of the abduction, whereas the vertical pitching–heaving appears later in the abduction phase. Both these motions combine to produce a strong and long-lasting tip vortex that stays attached to the tip through most of the abduction phase and produces a large magnitude of local surface normal force. Chordwise and spanwise curvature also allows the fin to orient this large local surface force into the forward direction, thereby achieving significant thrust through most of the abduction phase. It is worthwhile to note that typical engineered pitching–rolling foils that are rigid (Techet *et al.* 2005) only pitch and heave in one (vertical) plane and, therefore, do not have any means of simultaneously incorporating a similar motion in the spanwise direction.

The adduction phase is similar to the power phase of a paddling motion wherein the paddle is oriented so as to maximize its area normal to the free stream and accelerated in the direction of the flow. This brings up another interesting view of the kinematics and thrust production scheme adopted by the sunfish. There are typically two types of kinematics that can be used to generate forward thrust in a flow, flapping (pitching–heaving) and paddling, which are shown schematically in figure 9. One of the key differences between the two strokes is that whereas pitching–heaving can produce thrust during both phases (upstroke and downstroke), underwater paddling typically produces thrust during the backstroke and drag during the forward stroke. Furthermore, during the time taken to reorient the foil between the two phases, the foil is nearly stationary and presents a blockage to the oncoming flow, thereby generating drag. This is one key reason why the paddling type of stroke is generally considered to be less efficient than the flapping stroke for underwater propulsion. However, if a gait could be devised where the drag associated with the forward stroke and during foil

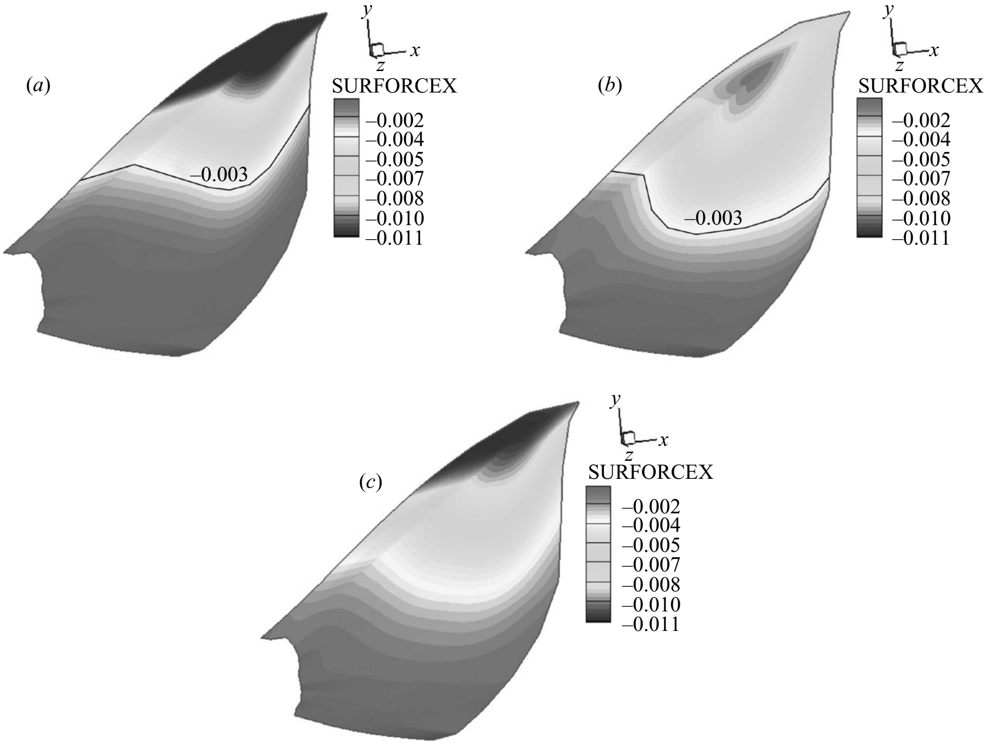

FIGURE 10. Contour of streamwise (x) component of the time-average, surface traction coefficient on the fin. Note that negative values of this quantity indicate thrust. (a) Average over the abduction phase. (b) Average over the adduction phase. (c) Time average over the complete cycle.

reorientation can be reduced or eliminated, then the backstroke can be effective and efficient at producing thrust. This is precisely what the fish fin is able to accomplish. In fact, it does even better than eliminating the drag associated with its forward (abduction) stroke. It uses a clever combination of fin kinematics and fin deformation to convert the forward stroke into one that is effectively a three-dimensional flapping stroke at the fin tip and manages to produce significant thrust during the forward stroke.

The significance of the fin tip region and the differences between abduction and adduction force production can be better understood by considering the contribution of various parts of the fin towards thrust production. In figure 10, we have plotted contours of the streamwise (x) component of the time mean, surface traction coefficient on the fin. In figures 10(a) and 10(b), we show the time means over the abduction and adduction phases, respectively, and in figure 10(c), we show this quantity for the entire cycle. A comparison of the contours plots for the abduction and adduction phases reveals some interesting insights. First, the thrust force during abduction is highly concentrated near the dorsal edge of the fin tip. This is in line with the discussion in the previous paragraphs, which indicates that the three-dimensional pitching–heaving motion that is produced by the fin in this region is primarily responsible for the production of thrust forces. In contrast, for the adduction phase shown in figure 10(b), the peak thrust forces are produced away from both the dorsal leading edge and the spanwise tip, which confirms that the forces during adduction are not a result of vortex-based mechanisms (similar to the abduction phase) which are strongest at the edges of the fins where these vortices are formed. Instead, forces during the adduction phase are likely associated with added-mass effects (Lighthill 1975) and correlated more closely with regions of large accelerations in the streamwise direction.

The second difference between the abduction and adduction phases is that during adduction, a larger portion of the fin contributes to thrust production. In order to establish this, we have identified one contour line corresponding to a value of −0.003, which is roughly one-fourth of the peak value. A comparison of this contour line for the abduction and adduction phases indicates that whereas during the abduction phase only about one-third of the fin surface produces significant thrust, during the adduction phase, close to half of the fin surface produces significant thrust. This further corroborates our assertion regarding the different mechanisms at play during the abduction and adduction phases of the fin stroke.

Finally, figure 10(*c*) shows the surface contours for the entire cycle, which is essentially an average of the abduction and adduction phases. As expected, the contours indicate that the region near the fin tip is the most crucial for thrust production. The ventral portion of the fin contributes very little to the thrust production and is, therefore, of little dynamical significance during steady swimming. However, examination of other gaits such as those associated with turns (Drucker & Lauder 2001) indicates that the ventral portion of the fin plays a more significant role there. It is also expected that the ventral portion of the fin is employed more effectively during fast starts and stops.

7. Conclusions

Numerical simulations have been used to study the hydrodynamics associated with the pectoral fin of a bluegill sunfish during steady forward swimming. The simulations are designed to complement the experimental investigation conducted by Lauder *et al.* (2006, 2007). The focus of the current paper is to examine in detail the production of forces by the fin, the three-dimensional vortex dynamics and to gain insight into the thrust production mechanisms.

The simulations reveal that the force components generated by the fin during its stroke are very different from those produced by a typical engineered rigid flapping foil. First, the fin produces significant thrust during all phases of the stroke, including when the fin reverses from abduction to adduction and vice versa. In contrast, rigid flapping foils produce drag peaks of varying magnitudes at stroke reversal. Second, the peak levels of transverse forces produced by the fin are similar to the peak thrust levels, whereas in engineered foils, these can be significantly higher. Furthermore, the mean values of the transverse forces are found to be quite small despite the fact that the abduction and adduction phases of the stroke are highly dissimilar. One important consequence of these force characteristics is that they allow the fish to swim with a highly reduced level of body oscillation, a factor that is likely important from the viewpoint of both visual field stabilization and dynamical stability of the fish body. Low magnitudes of peak forces also imply low levels of bending moments on the fin structure and joints. This is likely another factor that drives the kinematics of the fin, which itself is a delicate structure made of very flexible elements. The thrust coefficient and propulsive efficiency of the fin is found to match the best performing rigid flapping foil, except that the fish fin seems to produce this high level of thrust and efficiency at lower Strouhal numbers and lower amplitudes than the rigid flapping foils.

The motion of the fin creates a number of distinct vortex structures, including leading-edge and tip vortices, and these interact with each other in the wake to create a complex conglomeration of vortices that convect into the wake. A careful analysis of the fin motion, vortex dynamics and the surface force distribution indicates that during the abduction phase, the fin tip undergoes a complex, three-dimensional pitching–heaving motion that is driven by active chordwise deformation and passive spanwise deformation of the fin. This results in the formation of a strong and long-lasting attached tip vortex, which is responsible for producing most of the thrust during the abduction phase. During the adduction phase, the fin acts mostly like a paddle and moves backward rapidly while increasing its area normal to the incoming flow.

Thus, the simulations allow us to gain some new insights into the remarkable hydrodynamics and force production capabilities of the bluegill sunfish pectoral fin. One of the motivating factors for the current study is to use the above knowledge to develop a robotic pectoral fin that incorporates some of the key features of the bluegill pectoral fin and provides propulsive performance comparable to the fish fin. However, it is not clear at the outset as to what extent we need to replicate the complex structure of the fish fin. Thus, a method is needed that will allow us to establish those minimal features of the fin kinematics that are key to the propulsive performance. Furthermore, we also need to understand how the performance of this fin scales with key parameters such as Reynolds number and Strouhal number, since these are connected with factors such as sizing and frequency variation. All of these issues are addressed by Bozukurttas *et al.* (2009).

This research is funded by ONR MURI grant N00014-03-1-0897 monitored by Dr Thomas McKenna.

REFERENCES

Anderson, J. M., Streitlien, K., Barrett, D. S. & Triantafyllou, M. S. 1998 Oscillating foils of high propulsive efficiency. *J. Fluid Mech.* **360**, 41–72.

Blondeaux, P., Fornarelli, F., Guglielmini, L. & Triantafyliou, M. 2005 Vortex structures generated by a finite-span oscillating foil. *AIAA Paper* 2005-0084.

Bozukurttas, M., Mittal, R., Ddpmg, H., Lauder, G. V. & Madden, P. 2009 Low-dimensional models and performance scaling of a highly deformable fish pectoral fin. *J. Fluid Mech.* **631**, 311–342.

Buchholz, J. H. & Smits, A. J. 2006 On the evolution of the wake structure produced by a low-aspect-ratio pitching panel. *J. Fluid Mech.* **546**, 433–443.

Dabiri, J. O. 2005 On the estimation of swimming and flying forces from wake measurements. *J. Exp. Biol.* **208** (18), 3519–3532.

Dong, H., Mittal, R. & Najjar, F. M. 2006 Wake topology and hydrodynamic performance of low aspect-ratio flapping foils. *J. Fluid Mech.* **566**, 309–343.

Drucker, E. G. & Lauder, G. V. 2000 A hydrodynamic analysis of fish swimming speed: wake structures and locomotor force in slow and fast labriform swimmer. *J. Exp. Biol.* **203**, 2379–2393.

Drucker, E. G. & Lauder, G. V. 2001 Wake dynamics and fluid forces of turning maneuvers in sunfish. *J. Exp. Biol.* **204**, 431–442.

Drucker, E. G. & Lauder, G. V. 2002 Experimental hydrodynamics of fish locomotion: functional insights from wake visualization. *Integ. Comp. Biol.* **42**, 243–257.

Dyke, M. Van 1982 *An Album of Fluid Motion*. Parabolic.

Ellington, C. P., van den Berg, C., Willmott, A. P. & Thomas, A. L. R. 1996 Leading-edge vortices in insect flight. *Nature* **384**, 626–630.

Ghias, R., Mittal, R. & Dong, H. 2007 A sharp interface immersed boundary method for compressible viscous flows. *J. Comput. Phys.* **225**.

Hsieh, S. T. 2003 Three-dimensional hindlimb kinematics of water running in the plumed basilisk lizard (*basiliscus plumifrons*). *J. Exp. Biol.* **206**, 4363–4377.

Kern, R. & Varju, D. 1998 Visual position stabilization in the hummingbird hawk moth, macroglossum stellatarum l. I. Behavioural analysis. *J. Comp. Physiol.* A*: Neuroethol. Sens. Neural Behav. Physiol.* **182**, 225–237.

Koochesfahani, M. M. 1989 Vortical patterns in the wake of an oscillating airfoil. *AIAA J.* **27** (9), 1200–1205.

Lauder, G. V. & Madden, P. 2006 Learning from fish: kinematics and experimental hydrodynamics for roboticists. *Intl J. Autom. Comput*. **4**, 325–335.

Lauder, G. V. and Madden, P. G. A. (2007). Fish locomotion: kinematics and hydrodynamics of flexible foil-like fins. *Exp. Fluids* **43**, 641–653.

Lauder, G. V., Madden, P., Mittal, R., Dong, H. & Bozkurttas, M. 2006 Locomotion with flexible propulsors I: experimental analysis of pectoral fin swimming in sunfish. *Bioinsp. Biomim.* **1**, S25–S34.

Lewin, G. C. & Haj-Hariri, H. 2003 Modelling thrust generation of a two-dimensional heaving airfoil in a viscous flow. *J. Fluid Mech.* **492**, 339–362.

Lighthill, Sir J. 1975 *Mathematical Biofluiddynamics*. SIAM.

Milne, L. J. & Milne, M. 1965 Stabilization of the visual field. *Biol. Bull.* **128**, 285–296.

Mittal, R. 2004 Computational modelling in biohydrodynamics: trends, challenges, and recent advances. *IEEE J. Oceanic Engng* **29** (3), 595–604.

Mittal, R., Dong, H., Bozkurttas, M., Lauder, G. V. & Madden, P. 2006 Locomotion with flexible propulsors II: computational modelling of pectoral fin swimming in a sunfish. *Bioinsp. Biomim.* **1**, 35.

Mittal, R., Dong, H., Bozkurttas, M., Najjar, F., Vargas, A. & von Loebbecke, A. 2008 A versatile sharp interface immersed boundary method for incompressible flows with complex boundaries. *J. Comput. Phys.* **227**, 4825–4852.

Mittal, R. & Iaccarino, G. 2005 Immersed boundary methods. *Annu. Rev. Fluid Mech.* **37**, 239–61.

Press, W. H., Flannery, B. P., Teukolsky, S. A. & Vetterling, W. T. 2007 *Numerical Recipes: The Art of Scientific Computing*, 3rd edn. Cambridge.

Ramamurti, R. & Sandberg, W. C. 2001 Simulation of flow about flapping airfoils using a finite element incompressible flow solver. *AIAA J.* **39** (2), 253–352.

Ramamurti, R., Sandberg, W. C., Lohner, R., Walker, J. A. & Westneat, M. W. 2002 Fluid dynamics of flapping aquatic flight in the bird wrasse: three-dimensional unsteady computations with fin deformation. *J. Exp. Biol.* **205** (10), 2997–3008.

Soria, J. & Cantwell, B. J. 1993 Identification and classification of topological structures in free shear flows. In *Eddy Structure Identification in Free Turbulent Shear Flows* (ed. J. P. Bonnet & M. N. Glauser), pp. 379–390. Academic.

Stacoff, A., Steger, J., Stussi, E. & Reinschmidt, C. 1996 Lateral stability in sideward cutting movements. *Med. Sci. Sports Exerc.* **28**, 350–358.

Standen, E. M. & Lauder, G. V. 2005 Dorsal and anal fin function in bluegill sunfish lepomis macrochirus: three-dimensional kinematics during propulsion and maneuvering. *J. Exp. Biol.* **208**, 2753–2763.

Tangorra, J. L., Lauder, G. V., Madden, P. G., Mittal, R., Bozkurttas, M. & Hunter, I. W. 2008 A biorobotic flapping fin for propulsion and maneuvering. In *Proceedings of the IEEE International Conference on Robotics and Automation (ICRA)*, Pasadena, CA.

Techet, A. H., Lim, K. L., Hover, F. S. & Triantafylou, M. S. 2005 Hydrodynamic performance of a biologically inspired 3D flapping foil. In *Proceedings of 14th International Symposium on Unmanned Untethered Submersible Technology*, Durham, New Hampshire.

Triantafyllou, G. S., Triantafyllou, M. S. & Grosenbaugh, M. A. 1992 Optimal thrust development in oscillating foils with applications to fish propulsion. *J. Fluids Struc.* **7**, 204–224.

Triantafyllou, M. S., Hover, F. S. & Licht, S. 2003 The mechanics of force production in flapping foils under steady-state and transient motion conditions. *Tech. Rep.* MIT Department of Ocean Engineering, Testing Tank Facility Report 031903.

Tuncer, I. H., Walz, R. & Platzer, M. F. 1998 A computational study on the dynamic stall of a flapping airfoil. *AIAA Paper* 98-2519.

Udaykumar, H. S., Mittal, R., Rampunggoon, P. & Khanna, A. 2001 A sharp interface Cartesian grid method for simulating flows with complex moving boundaries. *J. Comput. Phys.* **174**, 345–380.

Walker, J. A. & Westneat, M. W. 1997 Labriform propulsion in fishes: kinematics of flapping aquatic flight in the bird wrasse, Gomphosus varius (labridae). *J. Exp. Biol.* **200**, 1549–1569.

Walker, J. A. & Westneat, M. W. 2000 Mechanical performance of aquatic rowing and flying. *Proc. R. Soc. Lond.* **267**, 1875–1881.

Ye, T., Mittal, R., Udaykumar, H. S. & Shyy, W. 1999 An accurate Cartesian grid method for simulation of viscous incompressible flows with complex immersed boundaries. *J. Comput. Phys.* **156**, 209–240.